

College of Medicine array Version 7.1) for Patient 3. Genechip Command Console Software (AGCC) 3.0.1 (Affymetrix) was used to summarize a probe information and the Partek suites v 6.4 software (Ryoka system, Tokyo, Japan) to determine genomic copy number and genotyping data for Patient 1 and Patient 2. Genome coordinates were according to the 36.1 build (March 2006) of the human reference genome at the UCSC database (<http://genome.ucsc.edu/>). This study was approved by the Institutional Review Board Committee of Hokkaido University Graduate School of Medicine, and written informed consents were obtained from the parents of the enrolled patients.

## Molecular Cytogenetic Analysis

A fluorescence in situ hybridization (FISH) was performed to confirm the deletions. Peripheral blood lymphocytes from two patients were used to prepare chromosomes, and RP11-277D10 BAC clone located in 5q31.3 overlapping region and RP11-701H24 BAC clone located in 15q11.2 for internal control were used as probes for Patient 1 and Patient 2, and RP11-831L1 BAC clone located in 5q31.3 was used for Patient 3. FISH was performed according to the standard procedure as described [Harada et al., 2002].

TABLE I. Clinical Features in Patients With 5q31.3 Deletion

	Our study			Shimajima et al. [2011]	
	Patient 1	Patient 2	Patient 3 (Decipher 248784)	Patient 1 (Decipher 253734)	Patient 2 (Decipher 4681)
Gender	Male	Female	Male	Male	Female
Current age (years)	6	12	1 3/12	1 6/12	8
Deletion	5q31.2q32	5q31.3	5q31.2q31.3	5q31.2q31.3	5q31.3
Size (Mb)	5.38	1.16	1.58	5.04	2.57
Origin	De novo (paternal)	De novo (maternal)	De novo	De novo (paternal)	De novo
Neonatal features					
Hypotonia	+	+	+	+	+
Feeding difficulties	+	+	+	+	+
Respiratory problems	Respiratory distress	Respiratory distress	Respiratory distress apnea	Recurrent pneumonia	na
Development					
Motor development delay	Severe	Severe	Moderate	Severe	Severe
Speech delay	Severe	Severe	na	na	+ (apraxic)
Neurological features					
Epilepsy	+	—	—	—	+ (Lennox Gastaut)
EEG epileptic discharges	+	—	—	+	+
Brain image (CT or MRI)	Brain volume loss	Delayed myelination	Simplified frontal gyral pattern and mild T2 high in the white matter	Brain volume loss delayed myelination	Brain volume loss delayed myelination
Facial features					
Low-set ears	—	—	—	+	+
Narrow forehead	+	+	+	+	+
Prominence of the metopic region	+	+	+	na	na
Sparse eyebrows	+	+	—	+	+
Telecanthus	+	+	+	+	+
Blepharoptosis	± (only left eye)	+	—	+	+
Downslanting palpebral fissures	—	+	—	—	+
Depressed nasal bridge	+	+	+	+	+
Short nose with upturned nostrils	—	—	—	+	+
High arched palate	+	+	+	+	+
Tented mouth	+	+	+	+	+
Marked philtrum	+	+	+	+	+
Micrognathia	+	+	+	na	na
Other					
Limb anomaly	—	—	—	Polydactyly (right hand)	na
Cardiac abnormality	—	—	+	+	na

na, not available.

## RESULT

Microarray analysis detected a 5.4 Mb deletion in 5q31.2q32 [arr 5q31.2-q32(138,899,205-144,275,780)x1] in Patient 1, a 1.2 Mb deletion in 5q31.3 [arr 5q31.3(139,219,584-140,379,177)x1] in Patient 2, and a minimum of 1.581 Mb and a maximum of 1.666 Mb [arr 5q31.2q31.3(138,011,434-139,592,820)x1] in Patient 3 (Fig. 3A). These deletions were subsequently confirmed by FISH (Fig. 3B). These deletions were not present in the parents of Patients 1 and 2 indicating their de novo origin. SNPs genotyping in the deleted region demonstrated that the deletion of Patient 1 was of paternal origin, and that of Patient 2 was of maternal origin (data not shown). The parental origin of the deletion in Patient 3 was not determined as this was lost to follow-up.

## DISCUSSION

Recently, Shimojima et al., 2011 reported on two patients who share a deletion of a region similar to the deleted region observed in our patients. The patients reported by Shimojima et al. demonstrated similar clinical features to our patients (Table I). We identified three additional patients with an overlapping deletion at 5q31.3. The patients showed strikingly similar clinical features including neonatal hypotonia, neonatal feeding difficulties that required tube feedings, respiratory distress, and severe developmental delay. They also exhibited facial dysmorphic features with narrow forehead, metopic prominence, lateral sparseness of the eyebrows, hypertelorism, depressed nasal bridge, open and tented mouth, marked philtrum and micrognathia (Table I). The new data support the

notion that 5q31.3 microdeletion represents a clinically recognizable syndrome.

The three patients presented here showed severe neonatal hypotonia, neonatal feeding difficulties, respiratory distress and characteristic facial features which were compatible with 5q31.3 microdeletion syndrome. Some, but not all of these clinical features and facial characteristics like the open-tented mouth and myopathic facial expression could be associated with the severe hypotonia of antenatal origin. Therefore, the causative genes of the 5q31.3 microdeletion syndrome may play a fundamental role in the proper development of the muscle tone and neuronal function. However, this possibility will require further elucidation with additional studies.

Shimojima et al. [2011] emphasized the significant delay of myelination demonstrated by brain MRI in patients with the 5q31.3 microdeletion syndrome. However, myelination delay was not common in this study although myelination delay was not able to be assessed in Patient 3 because MRI was taken during neonatal period. Rather, the brain MRI findings of three patients indicated variable abnormalities with mild volume loss of the brain, mild myelination delay, and a simplified frontal gyral pattern. Further collection of neuroimaging information will be valuable to delineate the developmental brain changes in patients with this syndrome.

Mosca et al. [2007] reported a patient carrying a microdeletion in 5q31.2 with intellectual disability (Fig. 4A). An additional patient with a microdeletion in 5q31.2 has been reported in the DECIPHER database (Fig. 4A). These patients have overlapping deletions and

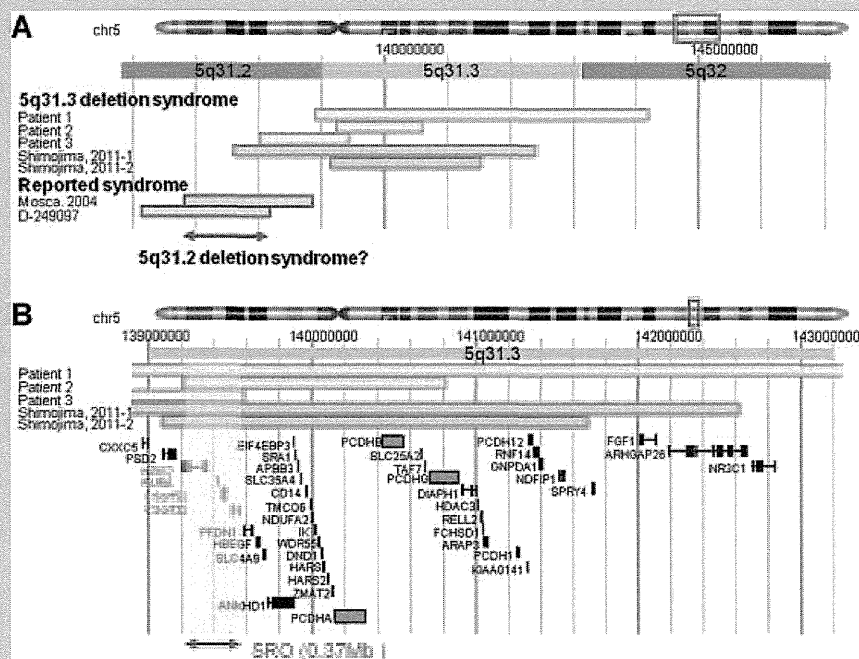


FIG. 4. A: Map of the overlapping deletions at 5q31.3. Shortest region of overlap (SRO) from three currently reported patients and two patients by Shimojima et al. [2011] defines 370kb region. Note that these deletions are not overlapped with microdeletions at 5q31.2. B: The SRO contains four RefSeq genes.

demonstrated similar clinical features although detailed information is not available for the latter patient. They show relatively mild developmental delay compared to patients harboring the 5q31.3 microdeletion, and the neonatal hypotonia is not very severe. These patients may represent a 5q31.2 microdeletion syndrome that is distinct from the 5q31.3 microdeletion syndrome.

Three patients with overlapping microdeletions in 5q31.3 are herein presented and compared to two previously reported patients (Fig. 4A). When the boundaries of the deletions observed in these patients were compared, the SRO, including only four RefSeq genes [Pruitt et al., 2007] (Fig. 4B) was narrowed to 370 kb in 5q31.3. Out of the four RefSeq genes, *NRG2* and *PURA* are well characterized functional genes, while the function of the remaining two genes, *C5orf53* and *C5orf32*, has not been characterized.

*NRG2* is one of the members of the neuregulin gene family that are related to growth and differentiation of neurons and glial cells [Falls, 2003], and its causative role has been pointed out by Shimojima et al. [2011].

*PURA* encodes a sequence-specific single-stranded DNA-binding protein [Khalili et al., 2003], and is related to pathogenic changes in fragile X-associated tremor/ataxia syndrome [Jin et al., 2007]. The role of the *PURA* protein in normal brain is not known. *Pura* deficient mice showed a neurologic phenotype consisting of tremor and spontaneous seizures [Khalili et al., 2003]. Thus, *PURA* may have a significant role in brain development. Therefore, *PURA* still remains a good candidate for the neurocognitive features observed in the 5q31.3 microdeletion syndrome, although the patients with 5q31.3 microdeletion do not demonstrate tremor or epilepsy which were cardinal features of *Pura*-deficient mice.

In conclusion, we have described three additional patients with 5q31.3 microdeletion syndrome, and confirmed that the syndrome is clinically discernible. The critical region for this chromosome abnormality has been narrowed down to a 370 kb region that encompasses *NRG2* and *PURA*. Further studies of infants with the syndrome may help to identify the genes in the SRO responsible for the clinical abnormalities in this microdeletion.

## ACKNOWLEDGMENTS

We are deeply grateful to the patients and their families who participate in this study. We also thank Prof. Tadashi Ariga for his thoughtful advice on this report, and Drs. Kyoko Takano and Takehiro Ishizuka at Shimada Center for Rehabilitation and Neurodevelopmental Intervention for their assistance. This study

was conducted by help of the DECIPHER database (Database of Chromosomal Imbalances and Phenotype in Humans using Ensemble Resources, <https://decipher.sanger.ac.uk>).

## REFERENCES

- Falls DL. 2003. Neuregulins: functions, forms, and signaling strategies. *Exp Cell Res* 284:14–30.
- Harada N, Takano J, Kondoh T, Ohashi H, Hasegawa T, Sugawara H, Ida T, Yoshiura K, Ohta T, Kishino T, Kajii T, Niikawa N, Matsumoto N. 2002. Duplication of 8p23.2: A benign cytogenetic variant? *Am J Med Genet* 111:285–288.
- Jin P, Duan R, Qurashi A, Qin Y, Tian D, Rosser TC, Liu H, Feng Y, Warren ST. 2007. *Purα* binds to rCGG repeats and modulates repeat-mediated neurodegeneration in a *Drosophila* model of Fragile X tremor/ataxia syndrome. *Neuron* 55:556–564.
- Khalili K, Del Valle L, Muralidharan V, Gault WJ, Darbinian N, Otte J, Meier E, Johnson EM, Daniel DC, Kinoshita Y, Amini S, Gordon J. 2003. *Purα* is essential for postnatal brain development and developmentally coupled cellular proliferation as revealed by genetic inactivation in mouse. *Mol Cell Biol* 23:6857–6875.
- Kubota T, Das S, Christian SL, Baylin SB, Herman JG, Ledbetter DH. 1997. Methylation-specific PCR simplifies imprinting analysis. *Nat Genet* 16:16–17.
- Li MM, Andersson HC. 2009. Clinical application of microarray-based molecular cytogenetics: An emerging new era of genomic medicine. *J Pediatr* 155:311–317.
- Miller DT, Adam MP, Aradhya S, Biesecker LG, Brothman AR, Carter NP, Church DM, Crolla JA, Eichler EE, Epstein CJ, Faucett WA, Feuk L, Friedman JM, Hamosh A, Jackson L, Kaminsky EB, Kok K, Krantz ID, Kuhn RM, Lee C, Ostell JM, Rosenberg C, Scherer SW, Spinner NB, Stavropoulos DJ, Tepperberg JH, Thorland EC, Vermeesch JR, Waggoner DJ, Watson MS, Martin CL, Ledbetter DH. 2010. Consensus statement: Chromosomal microarray is a first-tier clinical diagnostic test for individuals with developmental disabilities or congenital anomalies. *Am J Hum Genet* 86:749–764.
- Mosca AL, Callier P, Leheup B, Marle N, Jalloul M, Coffinet L, Feillet F, Valduga M, Jonveaux P, Mugneret F. 2007. Fortuitous FISH diagnosis of an interstitial microdeletion (5)(q31.1q31.2) in a girl suspected to present a cri-du-chat syndrome. *Am J Med Genet Part A* 143A:1342–1347.
- Pruitt KD, Tatusova T, Maglott DR. 2007. NCBI Reference Sequence (RefSeq): A curated non-redundant sequence database of genomes, transcripts and proteins. *Nucleic Acids Res* 35:D61–D65.
- Shimojima K, Isidor B, Le Caignec C, Kondo A, Sakata S, Ohno K, Yamamoto T. 2011. A new microdeletion syndrome of 5q31.3 characterized by severe developmental delays, distinctive facial features, and delayed myelination. *Am J Med Genet Part A* 155A:732–736.

## Visualization of the spatial positioning of the *SNRPN*, *UBE3A*, and *GABRB3* genes in the normal human nucleus by three-color 3D fluorescence in situ hybridization

Rie Kawamura · Hideyuki Tanabe ·  
Takahito Wada · Shinji Saitoh ·  
Yoshimitsu Fukushima · Keiko Wakui

Received: 13 February 2012 / Revised: 14 June 2012 / Accepted: 14 June 2012 / Published online: 17 July 2012  
© The Author(s) 2012. This article is published with open access at Springerlink.com

**Abstract** The three-dimensional (3D) structure of the genome is organized non-randomly and plays a role in genomic function via epigenetic mechanisms in the eukaryotic nucleus. Here, we analyzed the spatial positioning of three target regions; the *SNRPN*, *UBE3A*, and *GABRB3* genes on human chromosome 15q11.2–q12, a representative cluster of imprinted regions, in the interphase nuclei of B lymphoblastoid cell lines, peripheral blood cells, and skin fibroblasts derived from normal individuals to look for evidence of genomic organization and function. The positions of these genes were simultaneously visualized, and all inter-gene distances were calculated for each homologous chromosome

in each nucleus after three-color 3D fluorescence in situ hybridization. None of the target genes were arranged linearly in most cells analyzed, and *GABRB3* was positioned closer to *SNRPN* than *UBE3A* in a high proportion of cells in all cell types. This was in contrast to the genomic map in which *GABRB3* was positioned closer to *UBE3A* than *SNRPN*. We compared the distances from *SNRPN* to *UBE3A* (SU) and from *UBE3A* to *GABRB3* (UG) between alleles in each nucleus, 50 cells per subject. The results revealed that the gene-to-gene distance of one allele was longer than that of the other and that the SU ratio (longer/shorter SU distance between alleles) was larger than the UG ratio

---

Responsible Editor: Tatsuo Fukagawa

**Electronic supplementary material** The online version of this article (doi:10.1007/s10577-012-9300-5) contains supplementary material, which is available to authorized users.

R. Kawamura · T. Wada · Y. Fukushima · K. Wakui (✉)  
Department of Medical Genetics,  
Shinshu University School of Medicine,  
3-1-1 Asahi,  
Matsumoto, Nagano 390-8621, Japan  
e-mail: kwakui@shinshu-u.ac.jp

H. Tanabe  
Department of Evolutionary Studies of Biosystems,  
School of Advanced Sciences,  
The Graduate University for Advanced Studies (Sokendai),  
Shonan Village,  
Hayama, Kanagawa 240-0193, Japan

T. Wada  
Division of Pediatric Neurology, Kanagawa Children's  
Medical Center,  
2-138-4, Mutsukawa, Minami-ku,  
Yokohama 232-8555, Japan

S. Saitoh  
Department of Pediatrics and Neonatology, Nagoya City  
University Graduate School of Medical Sciences,  
1 Kawasumi, Mizuho-cho, Mizuho-ku,  
Nagoya 467-8601, Japan

(longer/shorter UG distance between alleles). The UG distance was relatively stable between alleles; in contrast, the SU distance of one allele was obviously longer than the distance indicated by the genome size. The results therefore indicate that *SNRPN*, *UBE3A*, and *GABRB3* have non-linear and non-random curved spatial positioning in the normal nucleus, with differences in the SU distance between alleles possibly representing epigenetic evidence of nuclear organization and gene expression.

**Keywords** Genome organization · Spatial positioning · 3D-FISH · *SNRPN* · Chromatin · Epigenetic

### Abbreviations

3C	Chromosome conformation capture
3D	Three dimensional
4C	3C-on chip or circular 3C
AS	Angelman syndrome
BAC	Bacterial artificial chromosome
CT	Chromosome territory
FBs	Skin fibroblasts
FISH	Fluorescence in situ hybridization
FPC	Fluorescence peak center
<i>GABRB3</i>	Gamma-aminobutyric acid (GABA) A receptor, beta 3
IQR	Interquartile range
LCLs	B lymphoblastoid cell lines
PB	Peripheral blood
PWS	Prader–Willi syndrome
<i>SNRPN</i>	Small nuclear ribonucleoprotein polypeptide N
<i>UBE3A</i>	Ubiquitin-protein ligase E3A

### Introduction

Recent experimental and computational advances have generated spatial information about nuclear architecture. We now know that the human genome, containing some 23,000 genes and 3.2 billion base pairs of DNA, is distributed among the 22 pairs of autosomes and two sex chromosomes, all of which are packed into the current chromatin compaction model. Interphase chromosomes are generally considered to be less condensed than their mitotic counterparts. To understand the complex workings of the genome in full, it is necessary to consider its three-

dimensional (3D) organization, rather than relying on linear information alone (Laster and Kosak 2010; Joffe et al. 2010). According to recent studies, higher-order chromatin organization and the spatial arrangement of genomic regions within the nucleus seem to play an important role in genome function via epigenetic mechanisms (Sproul et al. 2005; Lanctôt et al. 2007; Fraser and Bickmore 2007; Takizawa et al. 2008; Solovei et al. 2009; Ferrai et al. 2010; Egecioglu and Brickner 2011). Such findings were obtained by microscopic and, more recently, non-microscopic approaches. Microscopic techniques, such as 3D fluorescence in situ hybridization (3D-FISH) analysis, which although limited in resolution, provide spatial information such as physical distance, shape, and localization at the single-cell level (Shopland et al. 2006, Cremer and Cremer 2010; Crutchley et al. 2010). In 3D-FISH, radial positions and gene-to-gene distance are analyzed by the hybridization of probes to 3D-preserved nuclei. 3D-FISH studies have shown that individual chromosomes occupy discrete compartments called chromosome territories (CTs) that do not overlap with each other while adopting a preferential radial position within the nucleus. In many cell types, the radial organization of CTs is dependent on gene density or chromosome size. For instance, in rather spherically shaped nuclei, such as in lymphocytes, gene-dense chromosomes are located more internally while gene-poor chromosomes are located more peripherally (Croft et al. 1999; Boyle et al. 2001; Cremer et al. 2001; Tanabe et al. 2002). Bolzer et al. (2005) were the first to use 24-color 3D-FISH to simultaneously detect all chromosomes in human fibroblasts of interphase nuclei, presenting 3D maps of all CTs. Some genes change their nuclear location depending on gene activity (Lanctôt et al. 2007; Meaburn et al. 2007; Solinhac et al. 2011). For example, some genes loop out from their CT when active (Volpi et al. 2000; Williams et al. 2002; Mahy et al. 2002; Chambeyron and Bickmore 2004; Küpper et al. 2007; Ferrai et al. 2010). In this way, various genome organization phenomena have been microscopically observed.

Non-microscopic studies, such as chromosome conformation capture (3C) and 3C-based analysis, including 3C-on chip or circular 3C (4C), 3C-carbon copy (5C), chromatin interaction analysis by paired-end tag sequencing (ChIA-PET), and Hi-C, which although requiring large numbers of cells, provide spatial information of physical contact between

chromatin segments at a high resolution (Dekker et al. 2002; Simonis et al. 2006; Zhao et al. 2006; Dostie et al. 2006; Fullwood et al. 2009; Lieberman-Aiden et al. 2009; Handoko et al. 2011). In particular, 3C-based methods make it possible to determine genome-wide chromatin interaction frequency. In the 3C method, the frequency of spatial contacts between genomic loci is analyzed using formaldehyde cross-linking, ligation, and locus-specific PCR (Dekker et al. 2002). Several 3C and 3C-based studies have suggested that long-range chromatin interactions are involved in the epigenetic regulation of gene expression (Simonis et al. 2007; de Wit and de Laat 2012). For instance, the higher-order chromatin conformation at some loci differs between maternal and paternal alleles, and is correlated with the formation of CCCTC-binding factor (zinc finger protein) (CTCF)-dependent parent-of-origin specific loops (Murrell et al. 2004). Long-range looping interactions between genes can occur over a genomic distance of a few kb to tens of Mb (Simonis et al. 2006; Lieberman-Aiden et al. 2009; van Steensel and Dekker 2010). Furthermore, chromatin contacts not only occur between specific short functional elements, such as enhancers and promoters, but also over larger chromosomal domains, such as intrachromosomal (*cis*), interchromosomal (*trans*), and genomic environment contacts, when active genes share a transcription factory (Crutchley et al. 2010; van Steensel and Dekker 2010). Consequently, it seems that chromatin communicates as a spatial network in interphase nuclei. Such approaches complement each other by offering new insight into genomic spatial organization and function in the nucleus (Dekker 2008; Cremer and Cremer 2010; Crutchley et al. 2010, de Wit and de Laat 2012).

Despite previous findings, information on the relationship between genomic organization and function remains limited. In an attempt to further investigate, we focused on the following three genes in imprinted loci on 15q11.2–q13: *SNRPN*, which exhibits monoallelic (paternal) expression; *UBE3A*, which exhibits tissue-specific (e.g., brain) maternal expression; and *GABRB3*, which exhibits biallelic expression. Human chromosome 15q11–q13, a region subjected to genomic imprinting, is responsible for Prader–Willi syndrome (PWS) and Angelman syndrome (AS) (Horsthemke and Wagstaff 2008). The lack of a functional paternal copy of 15q11–q13 causes PWS, while the lack of a functional maternal copy of *UBE3A* causes AS. Several groups have studied the spatial organization of 15q11–

q13 using 3D image analysis. For example, Nogami et al. (2000) examined the relationship between *SNRPN* and chromosome territory in human myeloid leukemia HL60 cells. Teller et al. (2007) investigated the 3D distance between PWS/AS homologous regions in human lymphocytes, fibroblasts, and a gorilla lymphoblastoid cell line to examine the “chromosome kissing” hypothesis during the late S phase of interphase. Rauch et al. (2008) studied chromatin architecture within the PWS locus in a human lymphoblastoid cell line and fibroblast cell nuclei. They measured 3D distance between two of four probes located within 230 kb and analyzed chromatin compaction using computer simulations. However, they found no clearly detectable differences between the active and inactive PWS domains.

Although various observations have accumulated regarding the imprinted regions of PWS/AS, there are still insufficient data from a spatial viewpoint with regard to the relationship between higher-order chromatin configuration and gene activity. To the best of our knowledge, this is the first study to use three-color 3D-FISH to investigate spatial organization in the PWS/AS regions of three consecutive genomic regions—*SNRPN*, *UBE3A*, and *GABRB3*—in the nuclei of human B lymphoblastoid cell lines (LCLs), peripheral blood (PB) cells, and skin fibroblasts (FBs) derived from normal individuals.

In this study, we measured all 3D inter-gene distances between two of three target genes on each homologous chromosome in each cell to search for new evidence of genomic organization and function. As activity of the imprinted genes differs according to parental origin, simultaneous visualization of the genes by three-color 3D-FISH at the single-cell level was the only feasible approach, regardless of advances in 3C and 3C-based analyses. Here, we report both the regularity and differences in spatial organization among the three target regions in the nucleus. Our results provide possible epigenetic evidence of a relationship between gene-to-gene distance and genome function.

## Materials and methods

### Cell materials and preparation of specimens

Epstein–Barr virus-transformed human B LCLs, mononuclear cells isolated from whole heparinized

PB cells, and FBs from a healthy female individual with normal karyotype (F-LCL, F-PB, and F-FB), and LCLs and PB cells from a healthy male individual with normal karyotype (M-LCL and M-PB) were obtained for 3D-FISH analyses. Ethical approval for this project was granted by the Institutional Review Board of Shinshu University School of Medicine.

PB cells were isolated by Ficoll–Paque density gradient centrifugation, and red blood cells were removed using RBC Lysis Solution (Qiagen). PB cells were resuspended in saline at a concentration of approximately  $1 \times 10^7$  cells/mL.

LCLs and FBs in culture were synchronized for collection of large cell populations at G1 phase by the double-thymidine block method according to the standard procedure (Harper 2005) with minor modifications to analyze under conditions similar to PB cells at G0 phase. The releasing time was decided according to the doubling time of each cell type. LCLs were maintained in 10 % fetal bovine serum (FBS)/Roswell Park Memorial Institute 1640 (RPMI) medium at 37 °C in an atmosphere of 5 % CO<sub>2</sub>. Exponentially growing LCLs were blocked with excess thymidine (2 mM) for 12 h, and released for 12 h, then blocked again for 12 h, after that they were released for 15 h to synchronized G1 phase. LCLs were resuspended in 10 % FBS/RPMI at a concentration of approximately  $1 \times 10^7$  cells/mL. Suspended PB cells and LCLs from each subject were incubated at 37 °C for 1 h on poly-L-lysine-coated glass coverslips (24 × 60 mm). FBs were grown on coverslips with 10 % FBS/Dulbecco's modified Eagle's medium at 37 °C in 5 % CO<sub>2</sub> and were blocked with 2 mM thymidine for 12 h, then released for 12 h, and blocked again at 12 h, after that they were released for 15–15.5 h. The percentages of the cell cycle phase fractions of G0/G1, S, and G2/M in cultured cells were analyzed using FACS-Calibur and CellQuest Pro software (Becton Dickinson). More than 75 % G0/G1 cell populations of synchronized LCLs and FBs were used for 3D-FISH analyses.

All cell materials on coverslips were fixed and prepared to obtain 3D preserved cell nuclei according to the methods described previously (Cremer et al. 2001; Solovei et al. 2002) with slight modifications as follows. All coverslips with cells for 3D-FISH analysis were briefly washed with phosphate-buffered saline (PBS), fixed in 4 % paraformaldehyde (PFA) in 0.3 × PBS for 10 min, and washed again in PBS. For permeabilization, cells were treated with 0.5 % saponin and 0.5 % Triton X-100 in PBS for 20 min, washed in PBS, and after incubation

in 20 % glycerol in PBS for at least 30 min, subjected to repeated freeze–thaw cycles in liquid nitrogen five times. After washing cells again in PBS, they were incubated for 10 min in 0.1 N HCl, washed in PBS, incubated in 0.002 % pepsin in 0.01 N HCl at 37 °C for 2–6 min, and washed with 0.05 M MgCl<sub>2</sub> in PBS. Cells were postfixed with 1 % PFA in PBS for 10 min, washed in PBS, and then in 2 × SSC for 5 min. Cells on coverslips were stored at 4 °C in 50 % formamide in 2 × SSC until hybridization.

#### FISH probes

For measurement of gene-to-gene 3D distance in nuclei, we focused on one of the representative clusters in a human imprinting region that includes the *SNRPN*, *UBE3A*, and *GABRB3* genes mapped on 15q11.2–q12 within the region responsible for PWS and AS. *SNRPN* is a gene with paternal-only expression, *UBE3A* is the gene responsible for AS and shows maternal > paternal tissue-specific expression, and *GABRB3* is expressed from both parental alleles (Horsthemke and Wagstaff 2008).

Five human bacterial artificial chromosome (BAC) clones were selected by genome data base and purchased from BACPAC Resources at Children's Hospital and Research Center (Oakland) as three target regions of FISH probes. The probe S region including the *SNRPN* gene (RP11-98D02 and RP11-642G3), the probe U region including *UBE3A* (RP11-234J13), and the probe G region including *GABRB3* (RP11-48C8 and RP13-687N06) (Fig. 1a). Each BAC clone DNA was cultured and extracted using the standard alkaline lysis mini-prep protocol and tested for correct chromosomal location and the absence of signals on the pericentromeric region of one chromosome 15 homolog using metaphase spreads of LCLs from a PWS patient with a deletion of 15q11.2–q13 (PWS-del) by FISH. It was confirmed that the signal of each BAC clone was absent on one chromosome 15q homolog of the metaphase from PWS-del.

According to the primary structure of the human genome, the center of probe S to the center of probe U (SU region) is physically separated by about 451 kb, and the center of probe U to the center of probe G (UG region) is about 1,298 kb; thus SU region:UG region = 0.35:1. If chromosome condensation occurs over the entire chromosome, this proportion must remain the same.

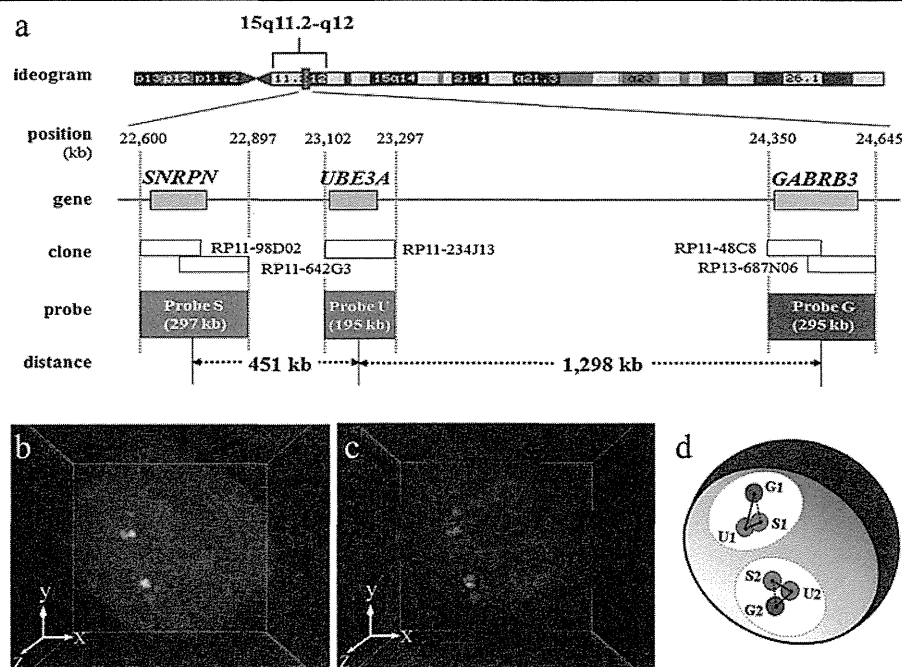


**Fig. 1** **a** Probe design for three-color 3D-FISH analysis of the target region on human chromosome 15q11.2–q12. **b**, **c** Visualization of three-color 3D-FISH on structurally preserved human LCL nuclei and an image of 3D distance measurements. FISH with probes S (green), U (red), and G (magenta), showing the *SNRPN*, *UBE3A*, and *GABRB3* genes, respectively. Nuclei were counterstained with DAPI (blue). 3D reconstruction (**c**) was

carried out from the captured image (**b**) obtained with Imaris software. Each signal spot was generated using the coordinate value from the FPC of each probe (i.e., probes S (green), U (red), and G (magenta)). Grid space, 1  $\mu\text{m}$ . **d** Diagram of the relative 3D intergenic distance measurements. Circles colored light yellow represent the assumed chromosome territories 15.  $S1U1 < S2U2$  distance

### Three-color 3D-FISH and probe detection

About 0.5  $\mu\text{g}$  of DNA from each probe was used for each hybridization. Probe S, probe U, and probe G were labeled using a nick-translation kit (Abbott) with SpectrumGreen-dUTP, SpectrumOrange-dUTP (Abbott), and Cy5-dCTP (GE Healthcare), respectively, according to the manufacturer's protocol, to measure gene-to-gene distances on each homologous chromosome 15.

3D-FISH and probe detection were performed according to protocols described elsewhere (Cremer et al. 2001; Solovei et al. 2002) with slight modifications.

Labeled probe DNAs of three target regions and Cot-1 DNA were mixed and subjected to ethanol precipitation, and then resuspended in hybridization solution (50 % formamide and 10 % dextran sulfate in 2 $\times$  SSC). The probes were predenatured at 80.5  $^{\circ}\text{C}$  for 6 min and placed on ice for 1 min. Denatured probes were applied to the coverslips on which fixed cells, covered with smaller coverslips (18 $\times$ 18 mm), and

sealed. The coverslip specimens were denatured at 75  $^{\circ}\text{C}$  for 5 min, and hybridization was performed in a moist chamber at 37  $^{\circ}\text{C}$  for 3–4 days. The specimens were washed in 2 $\times$  SSC, 0.1 $\times$  SSC at 60  $^{\circ}\text{C}$ , 4 $\times$  SSC with 0.2 % Tween 20, and 4 $\times$  SSC. Nuclear DNA was counterstained with 4',6-diamidino-2-phenylindole (DAPI) and the slides were mounted in Vectashield Antifade (Vector).

### Confocal microscopic Image

Nuclei were scanned with a four-channel laser-scanning confocal microscope (Zeiss LSM5 EXCITER; Carl Zeiss MicroImaging GmbH) equipped with a Plan-Apochromat 63 $\times$ /1.4 Oil DIC objective lens. For each optical section, images were collected sequentially for four fluorochromes (SpectrumGreen, SpectrumOrange, Cy5, and DAPI) using blue diode (405 nm), argon (488 nm), and helium-neon (543/633 nm) lasers, respectively.

To improve the signal-to-noise ratio, each sectional image obtained was an average of two successive scans. The focus  $z$ -step between sections was



0.364  $\mu\text{m}$ . Stacks of 12-bit grayscale two-dimensional images were obtained with  $512 \times 140$ – $320$  pixels in each channel.

Confocal image stacks were processed with the microscope operating software (ZEN; Carl Zeiss MicroImaging GmbH) and saved as LSM files. More than 50 nuclear images were captured from each cell material. Nuclei from cultured cells with singlet-singlet signals were adopted for calculation as in G1 phase of the cell cycle but with doublet-doublet or singlet-doublet signals for each probe, which were suspected to be in S or G2 phase, were not selected for capture.

#### Quantitative 3D evaluation

We specified the 3D coordinates of three target regions at a time in each cell and calculated the actual measured value between two of the three regions, and then determined the spatial organization among these regions in the nucleus. Various 3D measurement data, such as the coordinate value of the fluorescence peak center (FPC) of each signal/nucleus volume/sphericity/ellipsoid axis length  $x$ ,  $y$ , and  $z$ , were obtained using scientific 3D and 4D image processing and analysis software (Imaris, Imaris MeasurementPro, and ImarisCell; Bitplane).

Nuclei with sphericity of  $<0.5$ , suspected to be unable to maintain initially ordered 3D structures of the cells, were excluded from the calculation as the deformed nuclear shape leads to distortion of gene topology. Finally, 50 nuclei of each cell material were analyzed.

We measured the relative 3D gene-to-gene distance of three target regions, *SNRPN* (S), *UBE3A* (U), and *GABRB3* (G) genes at 15q11.2–q12 on each homologous chromosome 15 within the interphase nuclei, beginning with the 3D coordinate value of FPC of six fluorescent signals of the probes determined while checking 3D images of each nucleus simultaneously. We defined as “allele 1” on one of the homologous chromosomes 15 that had a shorter probe S-to-U distance (SU distance) than the other homologous chromosomes 15, and the FPC of probes S/U/G were defined as S1/U1/G1 on allele 1 in each nucleus. The FPC of probes S/U/G were defined as S2/U2/G2 on allele 2, which had a longer SU distance in each nucleus. Diagram of 3D distance measurements is shown in Fig. 1d. The shortest physical distances

between two of the three probes—SU distance, UG distance, and SG distance—on each homologous chromosome 15 were calculated from the  $x$ ,  $y$ , and  $z$  coordinates of the FPC of signals using the following equation and the spreadsheet application Excel (Microsoft Corporation).

$$\delta_{ij} = \sqrt{(x_i - x_j)^2 + (y_i - y_j)^2 + (z_i - z_j)^2}$$

\*any two loci  $i$  and  $j$

We also calculated angle U, which was defined as an internal angle formed by SU and UG sides, from the measurement data of distances SU, UG, and SG using the second cosine theorem with the following equation and the spreadsheet application Excel (Microsoft Corporation).

$$\theta = \cos^{-1} \frac{b^2 + c^2 - a^2}{2 \times b \times c}$$

\* $\theta$ : angle U, side  $b/c/a$ : distance SU/UG/SG

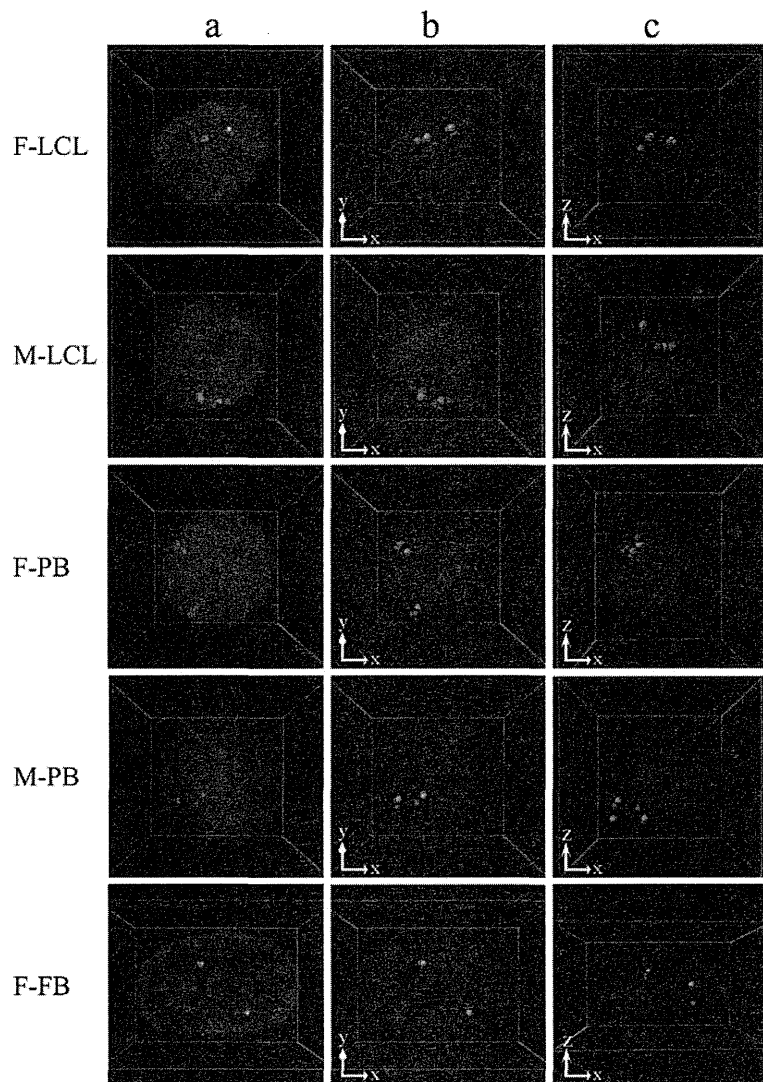
#### Statistical analysis

Fifty nuclei of each cell material were examined. We performed exploratory data analysis to find patterns in our results. Normality was assessed with the Shapiro–Wilk test. The distribution of measurements in a proportion of samples was not normal. Therefore, all measurements were analyzed using the nonparametric Mann–Whitney test between different cell types within the same individuals and between the same cell types among individuals. All statistical tests were two-sided, and  $P < 0.05$  was considered to indicate statistical significance. For multiple comparisons, significance levels were modified according to Bonferroni’s correction ( $\alpha$ ). All statistical analyses were performed with SPSS software version 18.0 (IBM).

#### Results

Three-color 3D-FISH was performed to measure gene-to-gene distance on 15q11.2–q12, on each homologous part of chromosome 15, within each interphase nucleus from the three different cell types examined (Figs. 1 and 2). The 3D gene-to-gene distance, angle U from 100 alleles in 50 nuclei, and the radius, volume, and sphericity of 50 nuclei in each subject are summarized in Table 1. Values were corrected according to the average  $x$ -,  $y$ - and  $z$ -axis radius to enable comparisons of gene-to-gene distance between different subjects.

**Fig. 2** Examples of three-color 3D-FISH results of projections and 3D reconstructions in typical nuclei from each subject. *Green/red/magenta* signals: probes S/U/G. 3D reconstructions in the *xy* (b) and *xz* direction (c) were obtained from the captured image (a) generated by Imaris software. Grid space, 1  $\mu\text{m}$



#### Gene-to-gene distance of the target regions and spatial positioning

A set of three signals for probes S, U, and G were readily distinguished on each allele in all cells. The interquartile range (IQR) and medians of the SU/UG/SG distance are shown in Table 1. Overall, the SG distance was shorter than the value obtained by summing the SU and UG distance.

As the volume of the nucleus varied between subjects, and since gene-to-gene distance is thought to be influenced by nuclear volume (as shown in Table 1), comparisons of distance were made after normalizing the average nuclear radius of the *x*-, *y*-, and *z*-axis in each subject (Fig. 3). The SU/UG/SG distance were

significantly different between LCLs, PB cells, and FBs of the same individual ( $P < 0.0005$ , UG and SG distances between F-LCLs and F-FBs;  $P = 0.004$ ,  $P = 0.007$ , respectively; Bonferroni's correction,  $\alpha < 0.008$ ), except for the SU distance between F-LCLs and F-FBs. There was no significant difference between identical cell types from different individuals for LCLs and PB cells (F-LCLs and M-LCLs; F-PB and M-PB cells) (Fig. 3).

Angle U, defined as the internal angle formed by the SU and UG sides, also varied in size, with the median angle being approximately  $60^\circ$  in all subjects (Table 1; Fig. 3). There was no significant difference between different cell types of the same individual (F-LCLs, F-PB cells, and F-FBs; M-LCLs and M-PB

**Table 1** 3D distances of SU/UG/SG and angle U in the nucleus calculated using the 3D coordinate values of the FPC of probe signals and the radius, volume, and sphericity of the nucleus

Subjects	Measured value median (IQR; $\mu\text{m}$ )			Measured value median (IQR)			
	Corrected value median <sup>a</sup> (IQR; %)			Angle U <sup>b</sup> (degree)	Radius <sup>c</sup> ( $\mu\text{m}$ )	Volume ( $\mu\text{m}^3$ )	Sphericity
	SU distance	UG distance	SG distance				
F-LCL	0.255 (0.170–0.366) 6.2 (4.0–8.6)	0.645 (0.436–0.864) 15.7 (10.4–20.6)	0.564 (0.352–0.771) 13.5 (8.2–18.3)	56 (34–73)	4.2 (4.0–4.3)	290 (264–318)	0.93 (0.91–0.94)
M-LCL	0.345 (0.248–0.523) 6.6 (4.8–10.0)	0.803 (0.571–1.000) 15.2 (11.2–19.1)	0.722 (0.504–0.898) 13.7 (9.5–17.6)	59 (41–86)	5.4 (5.2–5.5)	605 (531–637)	0.83 (0.77–0.88)
F-PB	0.439 (0.268–0.719) 8.3 (5.4–13.8)	0.945 (0.726–1.285) 18.7 (14.2–25.8)	0.895 (0.677–1.243) 17.7 (13.3–25.0)	59 (37–85)	5.0 (4.7–5.3)	515 (430–597)	0.93 (0.87–0.94)
M-PB	0.569 (0.326–1.068) 10.8 (6.7–18.6)	1.046 (0.759–1.434) 21.1 (15.0–26.6)	0.964 (0.68–1.324) 19.4 (13.7–26.0)	63 (34–88)	5.2 (4.5–5.7)	560 (372–710)	0.91 (0.88–0.94)
F-FB	0.423 (0.271–0.556) 6.6 (4.3–9.0)	0.806 (0.593–1.057) 12 (9.5–15.9)	0.674 (0.470–0.900) 9.9 (7.5–14.3)	53 (31–84)	6.1 (5.6–7.4)	683 (565–1152)	0.70 (0.65–0.75)

$n=100$  alleles, 50 nuclei from each subject

*IQR* interquartile range

<sup>a</sup> Median of corrected value by the radius (relative radius (in percent)). Measured value/radius  $\times$  100

<sup>b</sup> Internal angle formed by SU and UG sides

<sup>c</sup> Average of  $x$ -,  $y$ -, and  $z$ -axis radius

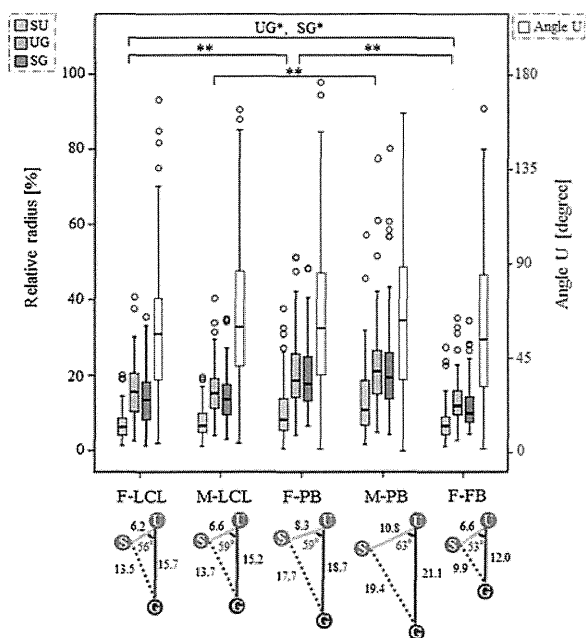


**Fig. 3** Gene-to-gene distance of SU/UG/SG and angle U for each subject. The *colored boxes* and *whisker plots* show the distributions of SU, UG, and SG gene distance (corrected value, relative radius), and the *red-lined boxes* and *whisker plots* show the distributions of angle U. Angle U is defined as the internal angle formed by the SU and UG sides. The *left axis* in the graph shows the relative radius and the *right axis* the angle U. The *box plots* summarize data obtained using the median, upper, and lower quartiles, as well as the range. *Boxes* represent the 25th to 75th percentiles (IQR). The *solid line* within the boxes indicates the median. *Lower* and *upper whiskers* show the 10th and 90th percentiles, respectively, of the distribution. *Open circles* indicate outliers. For the SU/UG/SG distance and the angle U, *P* values were obtained using the Mann–Whitney test between different cell types of the same individuals (F-LCL, F-PB, and F-FB; M-LCL and M-PB) and between identical cell types from different individuals (F-LCL and M-LCL; F-PB and M-PB). A *P* value < 0.008 was considered statistically significant after correcting for multiple comparisons (Bonferroni’s correction,  $\alpha = 0.05/6 = 0.008$ ; \**P* < 0.008; \*\**P* < 0.001; *n* = 100 alleles, 50 nuclei) The *bottom diagram* presents the summarized configuration of *SNRPN*, *UBE3A*, and *GABRB3* genes in the nucleus for each subject, cited according to the corrected median value of the SU/UG/SG distance and the angle U (Table 1)

cells), and between identical cell types from different individuals (F-LCLs and M-LCLs; F-PB and M-PB cells).

**Distance ratio between alleles and between regions**

We analyzed the 3D intergenic distance of three target genes between each homologous part of chromosome 15 for each allele in all subjects (Fig. 1d) to determine

differences between alleles of each target region (e.g., S1U1 vs. S2U2) (Fig. 4a) and between adjacent parts of the same chromosome (e.g., S1U1 vs. U1G1) (Fig. 4b) within 3D nuclei. The median distance of S1U1, S2U2, U1G1, and U2G2 is shown in Table 2.

The distance ratio was defined as:

$$\begin{aligned} \text{SU ratio} &= \text{longer SU} / \text{shorter SU distance} \\ \text{UG ratio} &= \text{longer UG} / \text{shorter UG distance} \end{aligned}$$

In all subjects, the median SU ratio was higher than the median UG ratio. The differences between the SU and UG ratios were significant in F-PBs and M-PB cells (*P* = 0.0004 and *P* = 0.0037, respectively; Bonferroni’s correction,  $\alpha < 0.0045$ ). There was no significant difference in the SU and UG ratio between different cell types of the same individual (F-LCLs, F-PB cells, and F-FBs; M-LCLs and M-PB cells) and between identical cell types from different individuals (F-LCLs and M-LCLs; F-PB and M-PB cells) (Fig. 4a).

According to the genomic coordinates, SU is 451 kb and UG is 1,298 kb, therefore SU:UG = 0.35:1. The median distance ratios were: S1U1/U1G1 = 0.32, S2U2/U2G2 = 0.48 in F-LCLs; S1U1/U1G1 = 0.35, S2U2/U2G2 = 0.61 in M-LCLs; S1U1/U1G1 = 0.28, S2U2/U2G2 = 0.58 in F-PB cells; S1U1/U1G1 = 0.34, S2U2/U2G2 = 0.82 in M-PB cells; and S1U1/U1G1 = 0.41, S2U2/U2G2 = 0.75 in F-FBs (Fig. 4b, c). There was no significant difference in allele 1 between different cell types of the same individual (F-LCLs, F-PB cells, and F-FBs; M-LCLs and M-PB cells) and between identical cell types from different individuals (F-LCLs and M-LCLs; F-PB and M-PB cells). Similarly, there was no significant difference in allele 2 (Fig. 4b).

**Discussion**

The 3D structure of the genome is organized non-randomly and plays a role in genome function via epigenetic mechanisms in the human nucleus. However, the genome is far more complex than can be explained by linear information alone. The present study was therefore performed to investigate how consecutive genes including imprinting genes are arranged spatially in human interphase nuclei with the aim of acquiring knowledge of genomic organization and function. We focused on *SNRPN*, showing paternal expression only, and contiguous *UBE3A* and *GABRB3* genes and examined whether specific higher-order chromatin

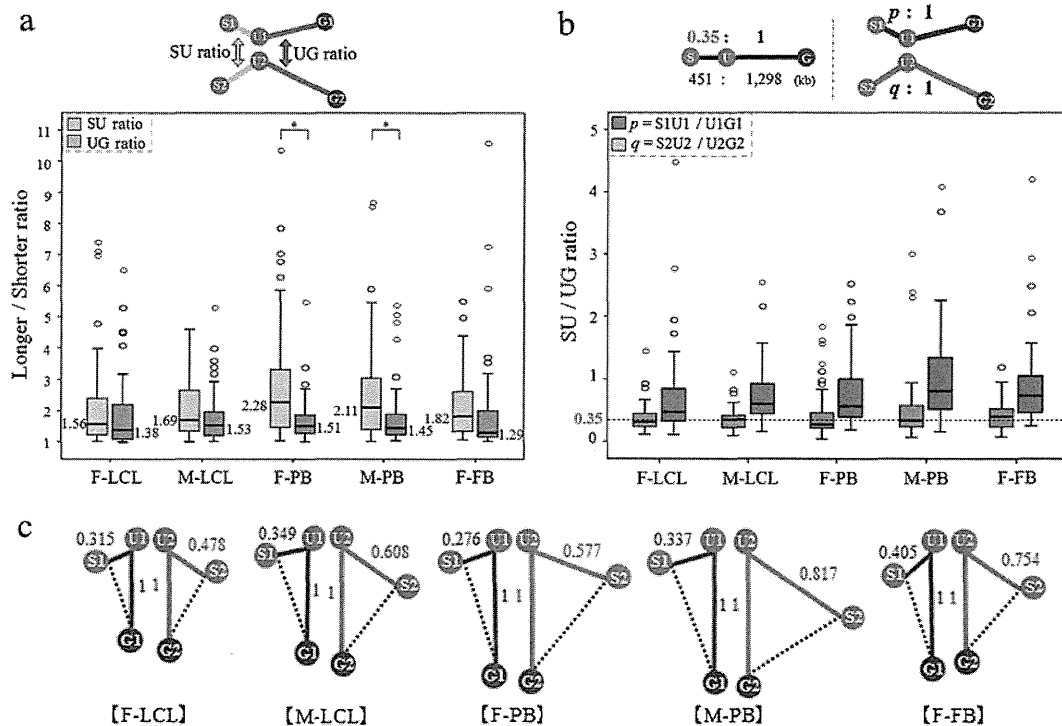


**Fig. 4** Distance ratios between alleles and between regions. **a** SU and UG distance ratios between alleles in each cell for each subject. Box and whisker plots show the distributions of the distance ratio for each subject. Distance ratios were calculated as follows: SU ratio (yellow lines in the top diagram)=longer SU/shorter SU distance; UG ratio (gray lines in the top diagram)=longer UG/shorter UG distance. For both the SU and UG ratios,  $P$  values were obtained using the Mann–Whitney test within each subject and between subjects (F-LCL, F-PB, and F-FB; M-LCL and M-PB; F-LCL and M-LCL; and F-PB and M-PB). A  $P$  value < 0.0045 was considered statistically significant after correcting for multiple comparisons (Bonferroni’s correction,  $\alpha=0.05/11=0.0045$ ; \* $P<0.004$ ;  $n=50$  nuclei). **b** SU/UG distance ratios of each allele for each subject. In the primary sequence of the human genome, SU:UG=451 kb:1,298 kb=0.35:1 (upper left diagram). Ratio of the distance of S1U1 when the distance of U1G1 was set to 1 (blue lines in the upper right diagram):  $p=S1U1/U1G1$  (blue box and whisker plots in the

graph). Ratio of the distance of S2U2 when the distance of U2G2 was set to 1 (red lines in the upper right diagram):  $q=S2U2/U2G2$  (red box and whisker plots in the graph). The dashed line in the plot shows 0.35. For  $p$  and  $q$ ,  $P$  values were obtained using the Mann–Whitney test between different cell types of the same individual (F-LCL, F-PB, and F-FB; M-LCL and M-PB) and between identical cell types from different individuals (F-LCL and M-LCL; F-PB and M-PB). A  $P$  value < 0.0045 was considered statistically significant after correcting for multiple comparisons (Bonferroni’s correction,  $\alpha=0.05/6=0.008$ ); no significant difference was observed ( $n=50$  nuclei). **c** Configuration of *SNRPN*, *UBE3A*, and *GABRB3* genes on homologous chromosomes in the nucleus for each subject drawn based on Table 2 and (b). Decimal fractions in blue indicate the median distance ratio of  $p$  as shown in (b). Likewise, decimal fractions in red denote the median distance ratio of  $q$ . The blue value “1” and red value “1” are not equal distances

organization could be observed microscopically using three-color 3D-FISH analysis in normal LCLs, PB cells, and FBs, all of which are used frequently for research (Figs. 1 and 2). Next, we evaluated regularity and differences in their spatial positioning (Figs. 3 and 4).

Gene-to-gene distances and spatial positioning of the target regions

We found that the *SNRPN*, *UBE3A*, and *GABRB3* genes had non-linear and non-random curved spatial

organization in the human nucleus (Fig. 3). Microscopic observations indicated that a distance of about 500 kb was measurable for comparison between homologous parts on the chromatin. Rauch et al. (2008) found no clearly detectable differences between the active and inactive PWS domains, as measured by 3D distance between two of four probes located within 230 kb. Our results indicated that *GABRB3* tended to be located closer to *SNRPN* than *UBE3A*, in contrast to the genomic map. Moreover, the median values of the internal angle  $U$  were calculated as 53–63° (Fig. 3).

**Table 2** Relative 3D distances of SU/UG/SG for each allele in the nucleus

Subjects	S1U1 distance (μm) Median (IQR)	U1G1 distance (μm) Median (IQR)	S1G1 distance (μm) Median (IQR)	S2U2 distance (μm) Median (IQR)	U2G2 distance (μm) Median (IQR)	S2G2 distance (μm) Median (IQR)
F-LCL	0.194 (0.124–0.273)	0.615 (0.429–0.765)	0.555 (0.360–0.740)	0.353 (0.251–0.448)	0.711 (0.440–0.933)	0.582 (0.350–0.893)
M-LCL	0.270 (0.166–0.334)	0.770 (0.597–0.936)	0.750 (0.638–0.878)	0.510 (0.356–0.601)	0.834 (0.547–1.038)	0.681 (0.433–0.901)
F-PB	0.273 (0.189–0.431)	0.908 (0.689–1.206)	0.856 (0.673–1.123)	0.652 (0.442–0.994)	0.987 (0.732–1.541)	0.968 (0.680–1.320)
M-PB	0.365 (0.228–0.594)	1.081 (0.756–1.424)	1.030 (0.754–1.319)	0.934 (0.549–1.187)	1.020 (0.781–1.437)	0.910 (0.581–1.331)
F-FB	0.271 (0.206–0.432)	0.852 (0.591–1.086)	0.692 (0.499–1.014)	0.531 (0.409–0.725)	0.803 (0.604–0.988)	0.657 (0.451–0.818)

*n* = 50 nuclei from each subject  
IQR interquartile range

4C analysis of human neuronal cells revealed that a PWS-imprinting center forms chromatin loops that contain key neurodevelopmental genes, including *GABRB3* (Yasui et al. 2011). Our results showing non-linear and non-random curved spatial organization of this region may support these findings.

Distance ratios between alleles and regions

We also found that gene-to-gene distance was not similar in size between alleles and regions (Fig. 4). The UG distance tended to be stable between alleles compared with the SU distance, even though the physical distance of UG is longer than that of SU according to the primary structure (Table 2). Figure 4a shows the differences in the SU and UG distance ratio between alleles; the SU ratio was larger than the UG ratio in all subjects. Comparison of the distance ratios between regions on the same allele revealed that the ratios of S2U2/U2G2 were >0.35, although those of S1U1/U1G1 were around 0.35 in all subjects (Fig. 4b). These results suggest that the S2U2 region may loosen more than the other region. It is generally believed that actively transcribed genes or genes poised for transcription are present in decondensed “open” chromatin configurations, while permanently silent genes are located within compact “closed” chromatin (Cremer et al. 2006). Regarding the PWS/AS region, Ohta et al. (1999) demonstrated that *SNRPN* chromatin is found in an open configuration exclusively on the paternal-derived allele. Thus, to summarize, the above results suggest that the degree of condensation seems to differ between homologous regions and adjacent regions of SU and UG.

Cell type specificity

The findings revealed that the spatial organization of the three target regions had a similar basic distribution in each of the three cell types examined. There were, however, subtle variations in gene-to-gene distance, which were dependent on cell type, even when from the same individual (Figs. 3 and 4). The *SNRPN* gene showed the same methylation pattern in a variety of tissues including LCLs, PB cells, and FBs (Glenn et al. 1996; Birney et al. 2010). Differences between cell types were related to the fact that PB cells and LCLs are in suspension, while FBs are adherent cells. The differences between PB cells and cultured cells were thought to be have been influenced by the cell cycle

since the PB cells were all in the G0 phase while the LCLs and FBs included G1, S, G2, and M phase cells, although the cultured cells were synchronized so the majority of the cell population was in the G1 phase. In addition, PB cells are composed of several kinds of mononuclear cells, in particular, T lymphocytes, B lymphocytes, and monocytes.

In this analysis, we examined 50 cells in each subject, and the obtained values of inter-gene distance displayed large variability among not only cycling cultured cells but also PB cells. Each fixed cell nucleus evaluated in the 3D-FISH analysis seemed to represent a snapshot in time of the higher-order structure and dynamics of chromatin (Teller et al. 2007; Cremer and Cremer 2010). Some investigations have shown that the movement of chromosomes and gene loci increases during early G1 (Walter et al. 2003) while other observations focusing on short-range chromatin motion suggest that local diffusional motion of chromatin is important in gene regulation (Soutoglou and Misteli. 2007). The probabilistic positioning of chromosomes can therefore show relatively large variation when single cells are compared. Furthermore, the 3D distance between genes in the nucleus is potentially influenced by chromatin compaction. Our results from the PB cells suggest that there is a range of chromatin compaction in the nucleus. Nishino et al. (2012) reported that human mitotic chromosomes consist predominantly of irregularly arranged nucleosome fibers, which they suggested exist in a similar state in the majority of active interphase nuclei. Our results will therefore help clarify chromatin structure in future studies.

3D-FISH using the three- or more-color approach is a powerful experimental tool for simultaneously visualizing the spatial positioning of multiple regions and comparing alleles in individual cells. However, it is also necessary to take into consideration the possible effects of the complicated process used to fix the cells and maintain their 3D structure for FISH analysis. It is difficult to preserve perfectly the 3D structure of nuclei from cells in suspension culture. Indeed, in this study, the volume of some nuclei could not be reproduced (data not shown).

In conclusion, the results of this study suggest that the *SNRPN*, *UBE3A*, and *GABRB3* loci have non-linear and non-random curved spatial organization in the nuclei of normal human cells. A distance of about 500 kb was measured microscopically for comparisons between homologous parts of chromatin within the nucleus. In addition, the differences in SU distance

between alleles and between regions on each chromosome 15 seem to represent new epigenetic evidence of nuclear organization and gene expression. Confirmation of the relationship between activity and the 3D distance of imprinted genes in the nucleus now remains in future studies.

If the epigenetic hypothesis is confirmed whereby intergenic distance is shown to vary depending on gene activity, it could lead to further research on the development of new diagnostic techniques for patients in whom mutations cannot be identified. This would be a breakthrough in our understanding of the pathological processes of certain diseases with unknown causes, as well as adding to basic research on chromatin structure, of which much remains unknown.

**Acknowledgments** We acknowledge the support of Research Center for Human and Environmental Sciences, Shinshu University, and Department of Laboratory Medicine, Shinshu University Hospital. We would also like to thank Dr. Yoshiharu Yokokawa (Shinshu University School of Health Sciences) for his helpful suggestion about statistical analysis. This work was supported by Grant-in-Aid for challenging Exploratory Research (24659156 to K.W.), Grant-in-Aid for Scientific Research (C) (18590311 and 20590328 to K.W., and 19590331 to T.W.) from Japan Society for the Promotion of Science, Grant-in-Aid for Scientific Research (21602002 and 23125505 to H.T.) from the Ministry of Education, Culture, Sports, Science and Technology of Japan, Grant for Research Projects from Hayama Center for Advanced Studies (to H.T.) support in part by the Center for the Promotion of Integrated Sciences (CPIS) of Sokendai (to H.T.), and for Intractable Disorder Conquest Research Grant from Ministry of Health, Labor and Welfare of Japan (to T.W. and to Y.F.).

**Open Access** This article is distributed under the terms of the Creative Commons Attribution License which permits any use, distribution, and reproduction in any medium, provided the original author(s) and the source are credited.

## References

- Birney E, Lieb JD, Furey TS, Crawford GE, Iyer VR (2010) Allele-specific and heritable chromatin signatures in humans. *Hum Mol Genet* 19:R204–R209
- Bolzer A, Kreth G, Solovei I et al (2005) Three-dimensional maps of all chromosomes in human male fibroblast nuclei and prometaphase rosettes. *PLoS Biol* 3:e157
- Boyle S, Gilchrist S, Bridger JM et al (2001) The spatial organization of human chromosomes within the nuclei of normal and emerin-mutant cells. *Hum Mol Genet* 10:211–219
- Chambeyron S, Bickmore WA (2004) Chromatin decondensation and nuclear reorganization of the HoxB locus upon induction of transcription. *Genes Dev* 18:1119–1130

- Cremer M, von Hase J, Volm T et al (2001) Non-random radial higher-order chromatin arrangements in nuclei of diploid human cells. *Chromosom Res* 9:541–567
- Cremer T, Cremer M, Dietzel S et al (2006) Chromosome territories—a functional nuclear landscape. *Curr Opin Cell Biol* 18:307–316
- Cremer T, Cremer M (2010) Chromosome territories. *Cold Spring Harbor Perspect Biol* 2:a003889
- Croft JA, Bridger JM, Boyle S et al (1999) Differences in the localization and morphology of chromosomes in the human nucleus. *J Cell Biol* 145:1119–1131
- Crutchley JL, Wang XQ, Ferraiuolo MA, Dostie J (2010) Chromatin conformation signatures: ideal human disease biomarkers? *Biomark Med* 4:611–629
- Dekker J, Rippe K, Dekker M, Kleckner N (2002) Capturing chromosome conformation. *Science* 295:1306–1311
- Dekker J (2008) Gene regulation in the third dimension. *Science* 319:1793–1794
- de Wit E, de Laat W (2012) A decade of 3C technologies: insights into nuclear organization. *Genes Dev* 26:11–24
- Dostie J, Richmond TA, Arnaout RA et al (2006) Chromosome conformation capture carbon copy (5C): a massively parallel solution for mapping interactions between genomic elements. *Genome Res* 16:1299–1309
- Egecioglu D, Brickner JH (2011) Gene positioning and expression. *Curr Opin Cell Biol* 23:338–345
- Ferrai C, de Castro IJ, Lavitas L, Chotalia M, Pombo A (2010) Gene positioning. *Cold Spring Harb Perspect Biol* 2:a000588
- Fraser P, Bickmore W (2007) Nuclear organization of the genome and the potential for gene regulation. *Nature* 447:413–417
- Fullwood MJ, Liu MH, Pan YF et al (2009) An oestrogen-receptor-alpha-bound human chromatin interactome. *Nature* 462:58–64
- Glenn CC, Saitoh S, Jong MTC et al (1996) Gene structure, DNA methylation, and imprinted expression of the human *SNRPN* gene. *Am J Hum Genet* 58:335–346
- Handoko L, Xu H, Li G et al (2011) CTCF-mediated functional chromatin interactome in pluripotent cells. *Nat Genet* 43:630–638
- Harper JV (2005) Synchronization of cell populations in G1/S and G2/M phases of the cell cycle. *Methods Mol Biol* 296:157–166
- Horsthemke B, Wagstaff J (2008) Mechanisms of imprinting of the Prader–Willi/Angelman region. *Am J Med Genet A* 146A:2041–2052
- Joffe B, Leonhardt H, Solovei I (2010) Differentiation and large scale spatial organization of the genome. *Curr Opin Genet Dev* 20:562–569
- Küpper K, Kölbl A, Biener D et al (2007) Radial chromatin positioning is shaped by local gene density, not by gene expression. *Chromosoma* 116:285–306
- Lancôt C, Cheutin T, Cremer M, Cavalli G, Cremer T (2007) Dynamic genome architecture in the nuclear space: regulation of gene expression in three dimensions. *Nat Rev Genet* 8:104–115
- Laster K, Kosak ST (2010) Genomic Pangea: coordinate gene regulation and cell-specific chromosomal topologies. *Curr Opin Cell Biol* 22:314–319
- Lieberman-Aiden E, van Berkum NL, Williams L et al (2009) Comprehensive mapping of long-range interactions reveals folding principles of the human genome. *Science* 326:289–293
- Mahy NL, Perry PE, Bickmore WA (2002) Gene density and transcription influence the localization of chromatin outside of chromosome territories detectable by FISH. *J Cell Biol* 159:753–763
- Meaburn KJ, Misteli T, Soutoglou E (2007) Spatial genome organization in the formation of chromosomal translocations. *Semin Cancer Biol* 17:80–90
- Murrell A, Heeson S, Reik W (2004) Interaction between differentially methylated regions partitions the imprinted genes *Igf2* and *H19* into parent-specific chromatin loops. *Nat Genet* 36:889–893
- Nishino Y, Eltsov M, Joti Y et al (2012) Human mitotic chromosomes consist predominantly of irregularly folded nucleosome fibres without a 30-nm chromatin structure. *EMBO J* 31:1644–1653
- Nogami M, Kohda A, Taguchi H et al (2000) Relative locations of the centromere and imprinted *SNRPN* gene within chromosome 15 territories during the cell cycle in HL60 cells. *J Cell Sci* 113:2157–2165
- Ohta T, Gray TA, Rogan PK et al (1999) Imprinting-mutation mechanisms in Prader–Willi syndrome. *Am J Hum Genet* 64:397–413
- Rauch J, Knoch TA, Solovei I et al (2008) Light optical precision measurements of the active and inactive Prader–Willi syndrome imprinted regions in human cell nuclei. *Differentiation* 76:66–82
- Shopland LS, Lynch CR, Peterson KA et al (2006) Folding and organization of a contiguous chromosome region according to the gene distribution pattern in primary genomic sequence. *J Cell Biol* 174:27–38
- Simonis M, Klous P, Splinter E et al (2006) Nuclear organization of active and inactive chromatin domains uncovered by chromosome conformation capture-on-chip (4C). *Nat Genet* 38:1348–1354
- Simonis M, Kooren J, de Laat W (2007) An evaluation of 3C-based methods to capture DNA interactions. *Nat Methods* 4:895–901
- Solinac R, Mompert F, Martin P et al (2011) Transcriptomic and nuclear architecture of immune cells after LPS activation. *Chromosoma* 120:501–520
- Solovei I, Walter J, Cremer M et al (2002) FISH on three-dimensionally preserved nuclei. In: Squire J, Beatty B, Mai S (eds) *FISH: a practical approach*. Oxford University Press, Oxford, pp 119–157
- Solovei I, Kreysing M, Lancot C et al (2009) Nuclear architecture of rod photoreceptor cells adapts to vision in mammalian evolution. *Cell* 137:356–368
- Soutoglou E, Misteli T (2007) Mobility and immobility of chromatin in transcription and genome stability. *Curr Opin Genet Dev* 17:435–442
- Sproul D, Gilbert N, Bickmore WA (2005) The role of chromatin structure in regulating the expression of clustered genes. *Nat Rev Genet* 6:775–781
- Takizawa T, Gudla PR, Guo L, Lockett S, Misteli T (2008) Allele-specific nuclear positioning of the monoallelically expressed astrocyte marker *GFAP*. *Genes Dev* 22:489–498
- Tanabe H, Müller S, Neusser M et al (2002) Evolutionary conservation of chromosome territory arrangements in cell



- nuclei from higher primates. *Proc Natl Acad Sci U S A* 99:4424–4429
- Teller K, Solovei I, Buiting K, Horsthemke B, Cremer T (2007) Maintenance of imprinting and nuclear architecture in cycling cells. *Proc Natl Acad Sci U S A* 104:14970–14975
- van Steensel B, Dekker J (2010) Genomics tools for unraveling chromosome architecture. *Nat Biotechnol* 28:1089–1095
- Volpi EV, Chevret E, Jones T et al (2000) Large-scale chromatin organization of the major histocompatibility complex and other regions of human chromosome 6 and its response to interferon in interphase nuclei. *J Cell Sci* 113:1565–1576
- Walter J, Schermelleh L, Cremer M, Tashiro S, Cremer T (2003) Chromosome order in HeLa cells changes during mitosis and early G1, but is stably maintained during subsequent interphase stages. *J Cell Biol* 160:685–697
- Williams RR, Broad S, Sheer D, Ragoussis J (2002) Subchromosomal positioning of the epidermal differentiation complex (EDC) in keratinocyte and lymphoblast interphase nuclei. *Exp Cell Res* 272:163–175
- Yasui DH, Scoles HA, Horike S et al (2011) 15q11.2-13.3 chromatin analysis reveals epigenetic regulation of *CHRNA7* with deficiencies in Rett and autism brain. *Hum Mol Genet* 20:4311–4323
- Zhao Z, Tavossidana G, Sjölander M et al (2006) Circular chromosome conformation capture (4C) uncovers extensive networks of epigenetically regulated intra- and inter-chromosomal interactions. *Nat Genet* 38:1341–1347

Editor's Summary

### Elucidating the Mechanism of Ataxia in Angelman Syndrome

Angelman syndrome is a neurodevelopmental disorder caused by loss of the ubiquitin E3 ligase Ube3a. A variety of symptoms, including severe developmental delay, speech impairment, epilepsy, and movement and balance problems, are associated with Angelman syndrome. In a new study, Egawa *et al.* investigate electrophysiological features of cerebellar dysfunction in a mouse model of Angelman syndrome. The authors report that extrasynaptic  $\gamma$ -aminobutyric acid type A (GABA<sub>A</sub>) receptor-mediated tonic inhibition decreases in cerebellar granule cells from the Ube3a-deficient Angelman mice. They then show that, normally, Ube3a binds to GABA transporter 1, a key modulator of extrasynaptic GABA, and controls its degradation in the mouse cerebellum. The Ube3a-deficient mice, however, showed a surplus of GABA transporter 1, resulting in decreased GABA concentrations in the extrasynaptic space and thus decreased tonic inhibition of cerebellar granule cells. Pharmacological compensation of decreased tonic inhibition by administering low doses of THIP, a selective agonist of extrasynaptic GABA<sub>A</sub> receptors, alleviated impaired motor function in the Ube3a-deficient mice. Thus, attenuated GABA transporter 1 degradation and a consequent decrease in tonic inhibition of cerebellar granule cells play a key role in the cerebellar dysfunction characteristic of Angelman syndrome. Pharmacologically increasing tonic inhibition with THIP may be a useful strategy for alleviating movement and balance problems in patients with this disease.

**A complete electronic version of this article** and other services, including high-resolution figures, can be found at:  
<http://stm.sciencemag.org/content/4/163/163ra157.full.html>

**Supplementary Material** can be found in the online version of this article at:  
<http://stm.sciencemag.org/content/suppl/2012/12/03/4.163.163ra157.DC1.html>

Information about obtaining **reprints** of this article or about obtaining **permission to reproduce this article** in whole or in part can be found at:  
<http://www.sciencemag.org/about/permissions.dtl>

# Decreased Tonic Inhibition in Cerebellar Granule Cells Causes Motor Dysfunction in a Mouse Model of Angelman Syndrome

Kiyoshi Egawa,<sup>1\*†</sup> Kyoko Kitagawa,<sup>2</sup> Koichi Inoue,<sup>1</sup> Masakazu Takayama,<sup>1</sup> Chitoshi Takayama,<sup>3</sup> Shinji Saitoh,<sup>4</sup> Tatsuya Kishino,<sup>5</sup> Masatoshi Kitagawa,<sup>2</sup> Atsuo Fukuda<sup>1†</sup>

Angelman syndrome is a neurodevelopmental disorder caused by loss of function of the *UBE3A* gene encoding a ubiquitin E3 ligase. Motor dysfunction is a characteristic feature of Angelman syndrome, but neither the mechanisms of action nor effective therapeutic strategies have yet been elucidated. We report that tonic inhibition is specifically decreased in cerebellar granule cells of *Ube3a*-deficient mice, a model of Angelman syndrome. As a mechanism underlying this decrease in tonic inhibition, we show that Ube3a controls degradation of  $\gamma$ -aminobutyric acid (GABA) transporter 1 (GAT1) and that deficiency of Ube3a induces a surplus of GAT1 that results in a decrease in GABA concentrations in the extrasynaptic space. Administering low doses of 4,5,6,7-tetrahydroisothiazolo-[5,4-c]pyridin-3-ol (THIP), a selective extrasynaptic GABA<sub>A</sub> receptor agonist, improves the abnormal firing properties of a population of Purkinje cells in cerebellar brain slices and reduces cerebellar ataxia in *Ube3a*-deficient mice in vivo. These results suggest that pharmacologically increasing tonic inhibition may be a useful strategy for alleviating motor dysfunction in Angelman syndrome.

## INTRODUCTION

Angelman syndrome is a neurodevelopmental disorder caused by a functional deficit in the brain-specific imprinted gene *UBE3A* (1, 2), which encodes the ubiquitin E3 ligase Ube3a (3) [also known as E6-associated protein (E6-AP)]. The major clinical manifestations consist of severe developmental delay, speech impairment, epilepsy, movement and balance problems, and characteristic behavior such as paroxysmal laughter (4). The mechanisms underlying Angelman syndrome-associated learning impairments have been revealed progressively (5–7) since the construction of a mouse model (*Ube3a*<sup>m-/p+</sup>) by targeted inactivation of maternal *Ube3a* (2, 8).

Abnormal movement and balance are characteristic features of Angelman syndrome that are largely attributed to cerebellar ataxia (9, 10), with about 35% of patients remaining nonambulatory at 5 years (11). However, despite its severe impact on patients, the mechanisms underlying the cerebellar ataxia in Angelman syndrome are still not clear. Several investigators have hypothesized that GABAergic dysfunction is involved in the neurological symptoms caused by Ube3a deficiency (9, 10). This is because patients with Angelman syndrome in whom there is deletion of chromosomes containing genes encoding  $\gamma$ -aminobutyric acid type A (GABA<sub>A</sub>) receptor  $\beta$ 3,  $\alpha$ 5, and  $\gamma$ 3 subunits show a more severe phenotype than do patients without these deletions (11, 12). However, paradoxically, the frequency and amplitude of phasic inhibitory postsynaptic currents (IPSCs) are normal in *Ube3a*<sup>m-/p+</sup> mice (7). These conflicting findings imply that another

form of inhibition, for example, tonic inhibition, might be compromised in Ube3a deficiency. Tonic inhibition is mediated by high-affinity, extrasynaptic GABA<sub>A</sub> receptors (13, 14) containing  $\alpha$ 6 and  $\delta$  subunits that are exclusively expressed in cerebellar granule cells (15).

The contribution of tonic inhibition to central nervous system (CNS) diseases is unclear. Recently, gain, rather than loss, of tonic inhibition has been shown to underlie the pathophysiology of epilepsy (16) and dysfunction after stroke (17), both of which are due to downregulation of GABA transporters. Studying the mechanisms of GABA transporter regulation is therefore likely to be essential for understanding the pathophysiology of Angelman syndrome. Here, we provide evidence that Ube3a binds to GABA transporter 1 (GAT1) and that Ube3a deficiency causes reduced degradation of GAT1. We further show that decreased concentrations of GABA, leading to decreased tonic inhibition of cerebellar granule cells, are the underlying cause of the cerebellar ataxia in Angelman syndrome.

## RESULTS

### Tonic inhibition is decreased in the cerebellar granule cells of *Ube3a*<sup>m-/p+</sup> mice

Recent studies using transgenic mice expressing a Ube3aYFP fusion gene have demonstrated that native Ube3a is maternally expressed in the cerebellar cortex, including the granule cell layer (18). Accordingly, we observed positive Ube3a immunoreactivity in the granule cell layer (particularly in presumed Golgi cells) of wild-type but not *Ube3a*<sup>m-/p+</sup> mice (fig. S1). Electron microscopic analysis did not reveal any apparent morphological changes in granule cell layer cytoarchitecture or synaptic architecture (fig. S2), indicating a functional rather than a structural disturbance in the mutant cerebellum.

Whole-cell voltage clamp recordings were conducted in cerebellar granule cells of acutely prepared cerebellar brain slices from mice at postnatal day (P) 25 to 28 (Fig. 1A). GABA<sub>A</sub> receptor-mediated tonic currents ( $I_{\text{tonic}}$ ) decreased by 34.1% in *Ube3a*<sup>m-/p+</sup> mice compared

<sup>1</sup>Department of Neurophysiology, Hamamatsu University School of Medicine, Hamamatsu 431-3192, Japan. <sup>2</sup>Department of Molecular Biology, Hamamatsu University School of Medicine, Hamamatsu 431-3192, Japan. <sup>3</sup>Department of Molecular Anatomy, School of Medicine, University of the Ryukyus, Nishihara 903-0215, Japan. <sup>4</sup>Department of Pediatrics and Neonatology, Nagoya City University Graduate School of Medical Sciences, Nagoya 467-8601, Japan. <sup>5</sup>Nagasaki University Center for Frontier Life Sciences, Nagasaki 852-8523, Japan.

\*Present address: Department of Neurology, Massachusetts General Hospital, 16th Street, CNY B-114, Charlestown, MA 02114, USA.

†To whom correspondence should be addressed. E-mail: cdh67560@par.odn.ne.jp (K.E.); axfukuda@hama-med.ac.jp (A.F.)

with wild-type mice (Fig. 1, A and C), as did the root mean square noise in the base holding current (Fig. 1D). Although the strength of tonic inhibition has been shown to increase during development (19),

in *Ube3a*<sup>m-/p+</sup> mice the reduction of  $I_{\text{tonic}}$  and base current noise was sustained into adulthood (Fig. 1, B and D), indicating that the decreased tonic inhibition at P25 to P28 was not a transient phenomenon.

Additional in vitro analyses were therefore performed in P25 to P28 mice.

Mean spontaneous IPSC (sIPSC) amplitude, rise time, and decay time were not significantly different between *Ube3a*<sup>m-/p+</sup> and wild-type cerebellar granule cells ( $P = 0.61, 0.48, \text{ and } 0.53$ , respectively; fig. S3, A to D). In accordance with previous reports, sIPSC frequency in cerebellar granule cells was low, usually less than 1 Hz (19), and was comparable between *Ube3a*<sup>m-/p+</sup> and wild-type mice ( $P = 0.69$ , Mann-Whitney  $U$  test; fig. S3E). These results indicate that in contrast to tonic inhibition, phasic inhibition in *Ube3a*<sup>m-/p+</sup> mice was not altered. We further evaluated evoked IPSCs (eIPSCs) in cerebellar granule cells. The eIPSC paired-pulse ratios did not significantly differ: interstimulus interval: 50 ms; wild-type:  $1.02 \pm 0.09$ ,  $n = 7$ ; *Ube3a*<sup>m-/p+</sup>:  $1.00 \pm 0.07$ ,  $n = 10$ ;  $P = 0.88$ . However, the eIPSC decay rate was significantly faster in *Ube3a*<sup>m-/p+</sup> mice ( $P < 0.05$ ; Fig. 1, E and F). Because eIPSCs are known to decay more slowly than sIPSCs in cerebellar granule cells owing to activation of extrasynaptic GABA<sub>A</sub> receptors (20), and because only eIPSC decay rate differed between mouse groups, events mediated by these receptors are likely specifically compromised in *Ube3a*<sup>m-/p+</sup> mice.

### Increased GAT1 activity underlies the decreased tonic inhibition in *Ube3a*<sup>m-/p+</sup> mice

Down-regulation of extrasynaptic GABA<sub>A</sub> receptors is a potential mechanism underlying decreased tonic inhibition. To verify this, we evaluated extrasynaptic GABA<sub>A</sub> receptor activation induced by exogenous GABA. Sustained current induced by pressure application with 600 nM GABA ( $I_{\text{GABA } 600 \text{ nM}}$ ), an applied concentration higher than the predicted ambient concentration of GABA in the extrasynaptic space (21), was not significantly different between groups ( $P = 0.48$ ), whereas that induced by endogenous ambient GABA was ( $I_{\text{tonic}}$ ; Fig. 2, A and B). Plotting the fold increase of  $I_{\text{GABA } 600 \text{ nM}}$  against  $I_{\text{tonic}}$  from both genotypes showed a clear inverse correlation that was well fitted by a Hill equation (Fig. 2B;  $R^2 = 0.783$ ). Because down-regulation of extrasynaptic GABA<sub>A</sub> receptors should result in less activation regardless of the source of GABA, these results suggest that the decreased tonic inhibition observed in *Ube3a*<sup>m-/p+</sup> mice is caused by lower ambient GABA concentrations rather than receptor down-regulation.

The ambient GABA concentration is tightly regulated by neuronal GAT1 and glial GATs (predominantly GABA transporter 4 in mice), which can take up GABA from the extrasynaptic space (17, 22, 23). Because maternally expressed *Ube3a* is not observed in astrocytes (18, 24), we evaluated the effect of GAT1

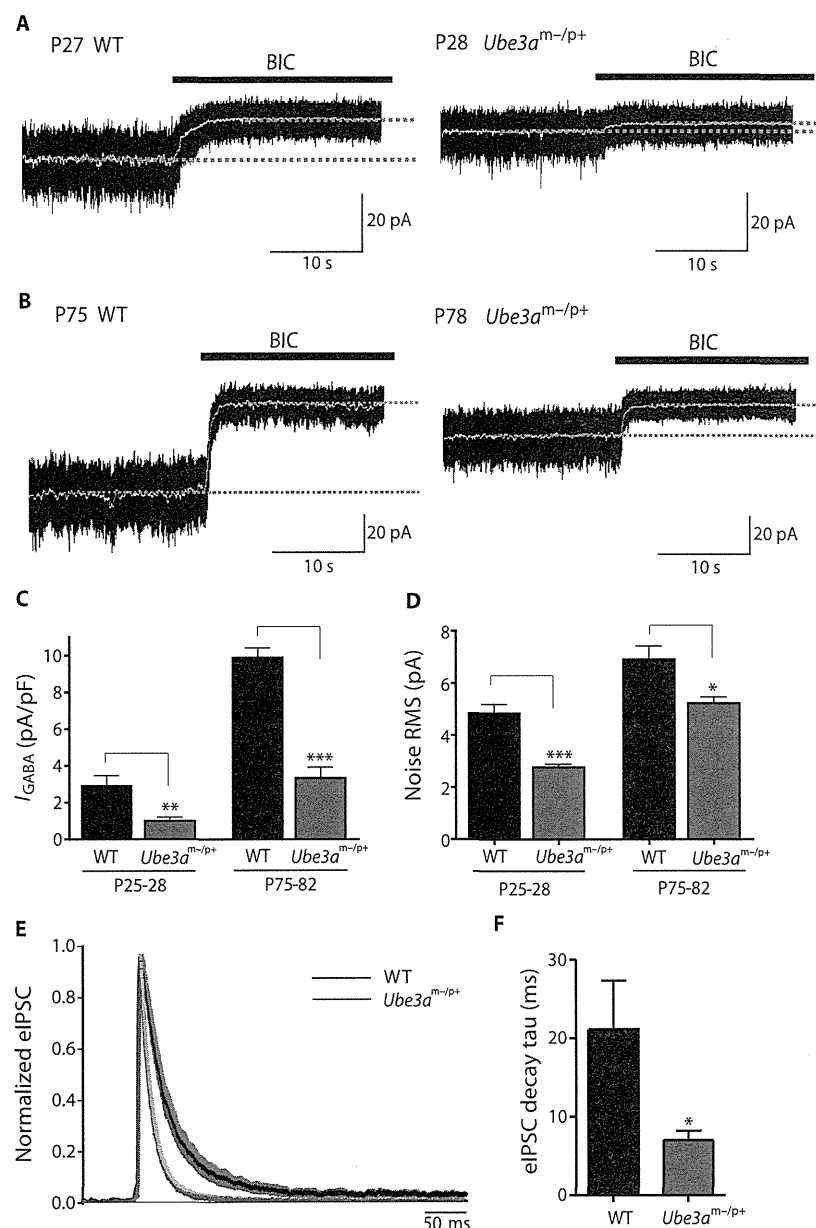


**Fig. 1.** Cerebellar tonic inhibition is decreased in *Ube3a*<sup>m-/p+</sup> mice. (A and B) Representative current traces of cerebellar granule cells from P25 to P28 (A) and P75 to P82 (B) wild-type (WT) and *Ube3a*<sup>m-/p+</sup> mice. Tonic GABA<sub>A</sub> receptor-mediated current ( $I_{\text{GABA}}$ ) was induced by focal application of 20  $\mu\text{M}$  bicuculline (BIC, black bars). To clarify the baseline, a 5-Hz, low pass-filtered overlay is given (gray traces) and extended (dotted gray lines). (C) Comparison of  $I_{\text{GABA}}$  density in WT (P25 to P28:  $n = 14$ , P75 to P82:  $n = 8$ ) and *Ube3a*<sup>m-/p+</sup> (P25 to P28:  $n = 15$ , P75 to P82:  $n = 8$ ) mice. (D) Comparison of root mean square (RMS) current noise of the base holding currents before application of BIC in the same mice as in (C). (E) Averaged traces of normalized eIPSCs in cerebellar granule cells from WT (black trace,  $n = 9$ ) and *Ube3a*<sup>m-/p+</sup> (red trace,  $n = 9$ ) mice. Pale colors indicate SEM. (F) Comparison of the eIPSC decay time constant (tau) shown in (E). \* $P < 0.05$ , \*\* $P < 0.01$ , \*\*\* $P < 0.001$ , unpaired  $t$  test. Data are means  $\pm$  SEM.